Inorg. Chem. **2008**, *47*, 8847−8858

Inorganic Chemistry
Article

Electroreduction of the Ruthenium Complex $[(bpy)_2Ru(tatpp)]Cl_2$ in Water: Insights on the Mechanism of Multielectron Reduction and Protonation of the Tatpp Acceptor Ligand as a Function of pH

Norma R. de Tacconi,[†] Reynaldo O. Lezna,[‡] Rungano Chitakunye,[†] and Frederick M. MacDonnell*,[†]

Department of Chemistry and Biochemistry, The University of Texas at Arlington, Arlington, Texas 76019-0065, INIFTA-CONICET, CC.16, Suc. 4, La Plata B1906ZAA, Argentina

Received May 19, 2008

The mononuclear ruthenium complex $[(bpy)_2Ru(tatpp)]^{2+}$ ($\mathbf{1}^{2+}$; bpy is 2,2′-bipyridine and tatpp is 9,11,20,22-tetraaza-tetrapyrido[3,2-a:2′3′-c:3″,2″-l:2‴,3‴]-pentacene) undergoes up to four reversible tatpp ligand-based reductions as determined by electrochemistry in aqueous solution. Specific redox and protonation states of this complex were generated by stoichiometric chemical reduction with cobaltocene and protonation with trifluoroacetic acid in acetonitrile. These species exhibit unique UV−visible absorption spectra, which are used to determine the speciation in aqueous media as a function of the potential during the electrochemical reduction. A combination of cyclic voltammetry, differential pulse voltammetry, and spectroelectrochemistry showed that the voltammetric reduction peaks are associated with two-electron/two-proton processes in which the details of stepwise electron transfer and protonation steps vary as a function of the pH. Spectroelectrochemistry performed during potential scans with and without a small superimposed sinusoidal potential waveform was used to examine the mechanistic details of this proton-coupled multielectron reduction process. Under basic conditions, the radical $[(bpy)_2Ru(tatpp^{\bullet-})]^{+}$($\mathbf{1}^{\bullet+}$) is the first electrogenerated species that converts to doubly reduced, single-protonated $[(bpy)_2Ru(Htatpp-)]^{+}$ ($H\mathbf{1}^{+}$) and doubly protonated $[(bpy)_2Ru(H_2tatpp)]^{2+}$($H_2\mathbf{1}^{2+}$) by subsequent electron-transfer (ET) and proton-transfer (PT) reactions. Partial dimerization of radical $\mathbf{1}^{\bullet+}$ is also observed in basic media. Neutral or acidic conditions favor an initial ET−PT reaction leading to the protonated, radical species $[(bpy)_2Ru(Htatpp^{\bullet})]^{2+}$ ($H\mathbf{1}^{\bullet 2+}$), which rapidly disproportionates to give $\mathbf{1}^{2+}$ and $H_2\mathbf{1}^{2+}$. This intermediate, $H\mathbf{1}^{\bullet 2+}$, is only observed when potential modulation is used in the spectroelectrochemical experiment. At more negative potentials, the doubly reduced complexes (e.g., $H_2\mathbf{1}^{2+}$, $H\mathbf{1}^{+}$) undergo a two-electron/two-proton reductions to give the quadruply reduced and protonated species $H_4\mathbf{1}^{2+}$ and/or $H_3\mathbf{1}^{+}$ throughout the pH range investigated. These species are also only detectable when potential modulation is used in the spectroelectrochemical experiment, as they rapidly comproportionate with $\mathbf{1}^{2+}$ in the bulk, leading to the regeneration of intermediate double-reduced species, $H_2\mathbf{1}^{2+}$.

Introduction

Interest in molecular photocatalysts designed to utilize solar energy for the production of fuels, such as hydrogen, has increased considerably in the past few years.[1−6] While the development of true water-splitting photocatalysts still faces a number of technical challenges, one central issue is matching the one-photon/one-electron nature of most molecular photoexcitations with the multielectron and multiproton requirements of important fuel-making reactions, such as hydrogen and oxygen evolution reactions. To date, only a few molecular photocatalysts have shown the ability to store multiple reducing or oxidizing equivalents via a photochemical process[7−15] even though such functionality is integral to natural photosystems. Proton transfer is also

* Author to whom correspondence should be addressed. E-mail: macdonn@uta.edu.
[†] The University of Texas at Arlington.
[‡] INIFTA-CONICET.

(1) Armaroli, N.; Balzani, V. *Angew. Chem., Int. Ed.* **2007**, *46*, 52–66.
(2) Eisenberg, R.; Nocera, D. G. *Inorg. Chem.* **2005**, *44*, 6779–6781.
(3) Alstrum-Acevedo, J. H.; Brennaman, M. K.; Meyer, T. J. *Inorg. Chem.* **2005**, *44*, 6802–6827.
(4) Dempsey, J. L.; Esswein, A. J.; Manke, D. R.; Rosenthal, J.; Soper, J. D.; Nocera, D. G. *Inorg. Chem.* **2005**, *44*, 6879–6892.
(5) Balzani, V.; Ceroni, P.; Maestri, M.; Saudan, C.; Vicinelli, V. *Top. Curr. Chem.* **2003**, *228*, 159–191.

10.1021/ic8009157 CCC: $40.75
Published on Web 09/12/2008

Chart 1

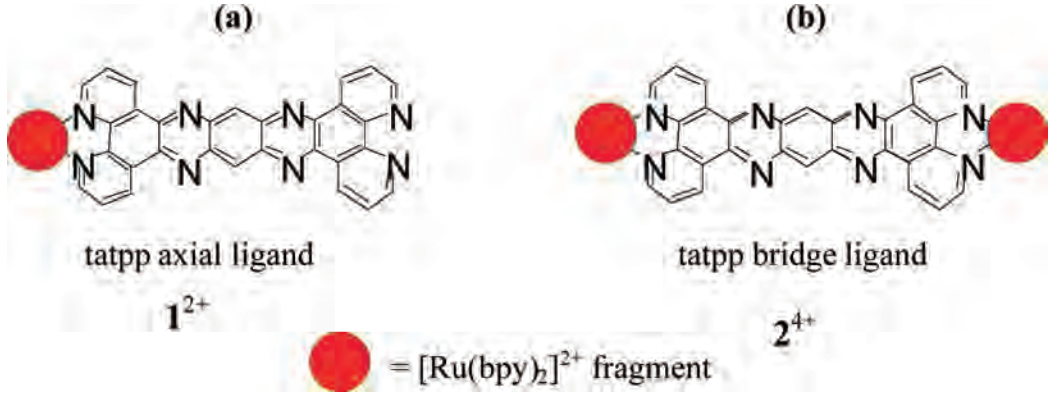

an essential feature of photoinduced electron-transfer processes in most natural light-activated energy storing processes[16,17] and similarly will play a central role in artificial photocatalysis. Toward this end, it has become apparent that a better understanding of the mechanisms by which multielectron and protonation processes occur is needed.[18,19]

We have previously shown that the dinuclear ruthenium(II) complexes, $[(bpy)_2Ru(tatpp)Ru(bpy)_2]^{4+}$ and $[(phen)_2Ru(tatpp)Ru(phen)_2]^{4+}$, are photochemically active, and both undergo two tatpp ligand-based reductions upon visible light irradiation in the presence of sacrificial donors.[7,20,21] The phenanthroline complex has also shown intriguing biological activity in that its doubly reduced form cleaves DNA by a mechanism that appears to involve a carbon-centered radical intermediate.[22] We have also shown that the related mononuclear complexes, $[(bpy)_2Ru(tatpp)]^{2+}$ ($\mathbf{1}^{2+}$) and $[(phen)_2Ru(tatpp)]^{2+}$ show similar redox processes in MeCN; however, this redox chemistry is complicated by the spontaneous formation of π-stacked assemblies in MeCN as well as the formation of σ-bonded dimers between radical species.[23]

Unlike the situation in MeCN, aggregation and radical dimerization are not the dominant processes for $\mathbf{1}^{2+}$ during the electroreduction in aqueous solution; instead, the complex remains largely unaggregated in this media, and the mechanistic details of electroreduction and protonation are more easily examined. In this work and with the assistance of differential spectroelectrochemistry, we are able to deconvolute some of the stepwise electron-transfer (ET) and proton-transfer (PT) steps that occur in an overall two-electron, two-proton process that is encompassed by a single voltammetric peak. By using the electrode as the electron source and the solvent as the proton source, we can decouple ET from PT,[24,25] and the overall mechanism can be shown to be a series of simple ET or PT reactions. In some cases, the products generated undergo subsequent homogeneous disproportionation or comproportionation reactions.[25,26]

Herein, we report on the speciation and mechanistic details of the multielectron electroreduction and protonation of complex $\mathbf{1}^{2+}$ (see Chart 1) in aqueous solution in the pH range from 10.5 to 2. The complex shows two main cathodic processes, C_1 and C_2, which were determined to be overall two-electron, two-proton processes. Spectroelectrochemistry performed in differential and integral modes was used to determine the mechanistic details of these two processes. The differential mode uses the imposition of a small potential modulation on a slow potential scan to give a differential reflectance signal sensitive to trace species (up to 10 ppm)[28,29] and allows the direct detection of many otherwise unobservable transient species. Their observation and role lead to a better understanding of the mechanism of multielectron storage in this class of photoactive complexes.

Experimental Section

The mononuclear ruthenium complex $\mathbf{1}[PF_6]_2$ and the related water-soluble $\mathbf{1}[Cl]_2$ were prepared by modifying a reported proce-

(6) Sun, L.; Hammarstrom, L.; Akermark, B.; Styring, S. *Chem. Soc. Rev.* **2001**, *30*, 36–49.
(7) Konduri, R.; Ye, H.; MacDonnell, F. M.; Serroni, S.; Campagna, S.; Rajeshwar, K. *Angew. Chem., Int. Ed.* **2002**, *41*, 3185–3187.
(8) Elvington, M.; Brewer, K. J. *Inorg. Chem.* **2006**, *45*, 5242–5244.
(9) Molnar, S. M.; Nallas, G.; Bridgewater, J. S.; Brewer, K. J. *J. Am. Chem. Soc.* **1994**, *116*, 5206–5210.
(10) Rosenthal, J.; Bachman, J.; Dempsey, J. L.; Esswein, A. J.; Gray, T. G.; Hodgkiss, J. M.; Manke, D. R.; Luckett, T. D.; Pistorio, B. J.; Veige, A. S.; Nocera, D. G. *Coord. Chem. Rev.* **2005**, *249*, 1316–1326.
(11) Heyduk, A. F.; Nocera, D. G. *Science* **2001**, *293*, 1639–1641.
(12) Esswein, A. J.; Veige, A. S.; Nocera, D. G. *J. Am. Chem. Soc.* **2005**, *127*, 16641–16651.
(13) Pfennig, B. W.; Mordas, C. J.; McCloskey, A.; Lockard, J. V.; Salmon, P. M.; Cohen, J. L.; Watson, D. F.; Bocarsly, A. B. *Inorg. Chem.* **2002**, *41*, 4389–4395.
(14) Chang, C. C.; Pfennig, B.; Bocarsly, A. B. *Coord. Chem. Rev.* **2000**, *208*, 33–45.
(15) Borgstrom, M.; Shaikh, N.; Johansson, O.; Anderlund, M. F.; Styring, S.; Akermark, B.; Magnuson, A. L. H. *J. Am. Chem. Soc.* **2005**, *127*, 17504–17515.
(16) Kirmaier, K.; Holten, D. *The Photosynthetic Bacterial Reaction Center - Structure and Dynamics*; Plenum: New York, 1988.
(17) Tommos, C.; Babcock, G. T. *Acc. Chem. Res.* **1998**, *31*, 18–25.
(18) Huynh, M. H.; Meyer, T. J. *Chem. Rev.* **2007**, *107*, 5004–5064.
(19) Cukier, R. I.; Nocera, D. G. *Annu. Rev. Phys. Chem.* **1998**, *49*, 337–369.
(20) Konduri, R.; de Tacconi, N. R.; Rajeshwar, K.; MacDonnell, F. M. *J. Am. Chem. Soc.* **2004**, *126*, 11621–11629.
(21) de Tacconi, N. R.; Lezna, R. O.; Konduri, R.; Ongeri, F.; Rajeshwar, K.; MacDonnell, F. M. *Chem. Eur. J.* **2005**, *11*, 4327–4339.
(22) Janaratne, T. K.; Yadav, A.; Ongeri, F.; MacDonnell, F. M. *Inorg. Chem.* **2007**, *46*, 3420–3422.
(23) de Tacconi, N.; Chitakunye, R.; Macdonnell, F. M.; Lezna, R. O. *J. Phys. Chem. A* **2008**, *112*, 497–507.
(24) Lebeau, E. L. B. R. A.; Meyer, T. J. *J. Am. Chem. Soc.* **2001**, *123*, 10535–10544.
(25) Trammell, S. A.; Wimbish, J. C.; Odobel, F.; Gallagher, L. A.; Narula, P. M.; Meyer, T. J. *J. Am. Chem. Soc.* **1998**, *102*, 13248–13249.
(26) Mastragostino, M.; Nadjo, L.; Saveant, J. M. *Electrochim. Acta* **1968**, *13*, 721–749.
(27) Wang, J.; Hoboken, N. J. *Analytical Electrochemistry*; Wiley-VCH: New York, 2006.
(28) Lezna, R. O.; de Tacconi, N. R.; Arvia, A. J. *J. Electroanal. Chem.* **1988**, *255*, 251–266.

dure[30] for the $[(phen)_2Ru(tatpp)]^{2+}$ complex using $[(bpy)_2Ru(1,10\text{-phenanthroline-5,6-dione})][PF_6]_2$[31] in place of $[(phen)_2Ru(1,10\text{-phenanthroline-5,6-dione}][PF_6]_2$.

Electrochemical data were obtained by using cyclic and differential pulse voltammograms (DPV) on a CHI620C electrochemical analyzer (CH Instruments, Austin, TX). Either glassy carbon (1.5-mm-diameter disk) or Au (1.0-mm-diameter disk) working electrodes from Cypress Systems were used. Immediately before use, the electrodes were polished to a mirror finish with wet alumina (Buehler, 0.05 μm), followed by rinsing with Millipore Milli-Q water and sonication. A Pt wire and a Ag/AgCl reference electrode (Cypress, model EE009) were used as counter and reference electrodes, respectively. The electrolyte solutions were prepared from a NaH_2PO_4/0.1 M K_2HPO_4 buffer; the pH was adjusted with 0.5 M NaOH or 0.5 M H_3PO_4 with the assistance of a standard glass electrode and a pH meter. Prior to each measurement, solutions were deoxygenated by bubbling argon. This atmosphere was maintained over the electrochemical solution throughout the course of the experiment. All experiments pertain to the laboratory ambient temperature (20 ± 2 °C).

Cobaltocene and trifluoroacetic acid (TFA), both from Alfa Aesar, were used as received. All redox and protonation titrations were carried out in a nitrogen atmosphere glovebox using stock solutions of $\mathbf{1}[PF_6]_2$ (10^{-4} M), $Co(Cp)_2$ (0.01 M), and TFA (0.01 M). Compounds $\mathbf{1}^{\bullet+}$ and $\mathbf{1}^0$ were generated by adding 1 and 2 equiv of $Co(Cp)_2$, respectively. The protonated species were generated by the stoichiometric addition of TFA to solutions of $\mathbf{1}^{\bullet+}$ and $\mathbf{1}^0$.

Two UV−visible spectroelectrochemical configurations were used: (a) Transmittance spectroelectrochemical measurements were performed during a slow potential scan (5 mV/s) in a quartz thin-layer compartment containing a gold minigrid as the working electrode. This compartment is placed inside a 1-cm-path cuvette containing ca. 0.5 mL of a $\mathbf{1}^{2+}$ solution (100−200 μM). The $\mathbf{1}^{2+}$ solution filled the thin-layer space by capillary action, and this liquid thin layer was spectroscopically probed as a function of the electrode potential by using a diode array spectrometer (Hewlett-Packard model 8453). The counter electrode (platinum wire) and the Ag/Ag^+ quasi-reference electrode were laterally placed in the quartz cuvette next to the thin-layer compartment.

(b) Reflectance measurements, using a mirror-polished gold electrode, were performed without and with superimposed potential modulation. In the first case, the reflectance (R) data were collected with an EG&G/PAR Optical Multichannel Analyzer during a slow potential scan (5 mV/s), the data being presented as $\Delta R/R$ versus potential at selected wavelengths. The reflectance changes, $\Delta R = R - R_0$, were measured, in this case, with respect to the system reflectance at the initial potential (R_0), where no reactions are taking place. In the second case, differential reflectivity in the form of $\delta R/R$ potential profiles (called hereafter DR) were recorded on a slow potential scan with superimposed, small-amplitude sinusoidal waveform (potential modulation). Monochromatic light (the wavelength chosen to be characteristic of the species being probed) is reflected off of the working electrode, focused on a photomultiplier operating at a constant current set by a feedback system and a programmable power supply. AC voltammetry was used along with DR measurements. The rectified AC current and optical AC response (normally, the in-phase component) in response to a small-amplitude sinusoidal potential perturbation (ca. 5 mV_{p-p}, 11 Hz) were monitored, after demodulation with a lock-in amplifier, as a function of the electrode potential.

Results

Figure 1 shows the structures and relationships of the various reduced and protonated species obtainable during the electroreduction of a $\mathbf{1}^{2+}$ aqueous solution. ET reactions are listed vertically and PT reactions horizontally. Although the speciation seen during the electroreduction of $\mathbf{1}^{2+}$ also reveals some side reactions, which we attribute to partial aggregation, radical dimerization, and possible comproportionation reactions, for clarity, these "side reactions" are omitted from Figure 1 and are only addressed in the discussion. Also included in Figure 1 is the notation used to identify the various redox and protonation states of the parent complex $\mathbf{1}^{2+}$.

A. Voltammetric Behavior of $\mathbf{1}^{2+}$ in Buffered Aqueous Solutions at Different pHs. The DPVs for $\mathbf{1}^{2+}$ in basic, neutral, and acidic buffered aqueous solutions are shown in Figure 2. The four voltammograms show two main peaks, C_1 and C_2, which shift toward more positive potentials with decreasing pH, as would be expected for proton-coupled redox processes. At pH 10.5, peak C_1 is a composite peak that shows a small shoulder coinciding with the reduction potential seen in the $\pi-\pi$ stacked dimer, $\pi\text{-}\{\mathbf{1}\}_2^{4+}$, in acetonitrile.[23] At a lower pH, this distinct shoulder is absent; however, the peak broadens, especially at pH < 7, indicative of multiple redox processes with close potentials. The shape of peak C_2 is less complex than that of peak C_1 and shows also a clear shift toward a more positive potential as the pH is lowered. Figure 3 shows that the peak potentials for C_1 and C_2 shift linearly as a function of pH. In this case, the peak potentials, E_{C1} and E_{C2}, are related to the respective half-wave potentials $E_{1/2}$ by the following equation:

$$E_{Cx} = E_{1/2} - \Delta P/2 \quad (x = 1 \text{ or } 2) \tag{1}$$

where ΔP is the DPV pulse amplitude (i.e., 50 mV for the data in Figure 2).[32] The slopes for the two lines in Figure 3 give values of 59 and 64 mV/pH for peaks C_1 and C_2, respectively, which is expected for Nernstian behavior. In general, a redox couple involving m protons and n electrons is expected to have a half-wave potential varying by $59(m/n)$ per unit of pH. As the slopes for complex $\mathbf{1}^{2+}$ are close to 59 mV/pH, these processes are both either $1e^-/1H^+$ or $2e^-/2H^+$ coupled processes.[33−37] Spectroelectrochemical data support the latter (vide infra).

B. Spectral Characterization of Reduced and Protonated Species of Complex $\mathbf{1}^{2+}$. In situ stoichiometric chemical reduction and protonation were used to chemically generate a number of the complexes shown in Figure 1.

(29) Sagura, T. In *Advances in Electrochemical Science and Engineering*; Alkire, R., Kolb, D., Lipkowski, J. P. R., Eds.; Wiley-VCH Verlag GmbH & Co KGaA: New York, 2006; Vol. *9*, pp 47−93.
(30) Wärnmark, K.; Thomas, J. A.; Heyke, O.; Lehn, J.-M. *Chem. Commun.* **1996**, 701–702.
(31) Bolger, J.; Gourdon, A.; Ishow, E.; Launay, J.-P. *Inorg. Chem.* **1996**, *35*, 2937–2944.
(32) Parry, E. P.; Osteryoung, R. A. *Anal. Chem.* **1965**, *37*, 1634.
(33) Laviron, E. *J. Electroanal. Chem.* **1983**, *146*, 15.
(34) Laviron, E. *J. Electroanal. Chem.* **1984**, *164*, 213–227.
(35) White, J. H.; Soriaga, M. P.; Hubbard, A. T. *J. Electroanal. Chem.* **1985**, *185*, 331.
(36) Wipf, D. O.; Wehemeyer, K. R.; Wightman, R. M. *J. Org. Chem.* **1986**, *51*, 60.
(37) Rüssel, C.; Jaenicke, W. *J. Electroanal. Chem.* **1978**, *88*, 193.

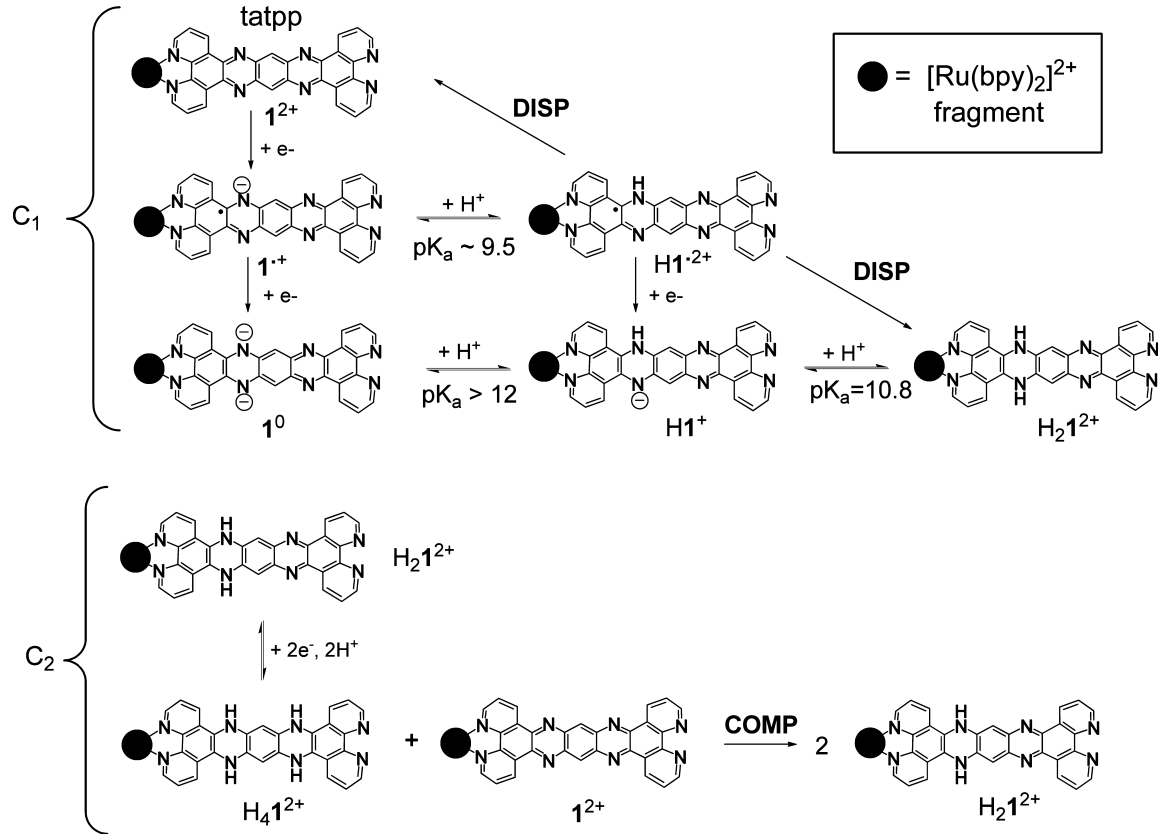

Figure 1. Schematic summary of the pH effect on the redox speciation and protonation occurring during the tatpp ligand electroreduction of complex $\mathbf{1}^{2+}$ in buffered aqueous media. The scheme is divided into two parts, C_1 and C_2, corresponding to the two main electroreduction peaks. The electron tranfer processes are presented vertically, while protonation/deprotonation processes are shown horizontally. A disproportionation reaction (DISP) is also indicated. For the sake of clarity, the partial dimerization of $\mathbf{1}^{+}$ was not included in this scheme and is deferred to the Discussion section of the paper.

These reactions were performed in dry MeCN to control the proton stoichiometry. Figure 4 shows the absorption spectra of $\mathbf{1}^{2+}$, $\mathbf{1}^{\bullet+}$, and $\mathbf{1}^{0}$ and the related protonated species $\mathbf{H1}^{\bullet 2+}$, $\mathbf{H1}^{+}$, and $\mathbf{H_21}^{2+}$ as obtained from titration with cobaltocene and trifluoroacetic acid. The data are presented in separated frames with the reduced nonprotonated species at the top and the protonated species at the bottom. Cobaltocene is a strong one-electron reducing agent ($E_0 = -1.0$ V vs Ag/AgCl in acetonitrile)[38] and therefore thermodynamically capable of generating both $\mathbf{1}^{\bullet+}$ and $\mathbf{1}^{0}$.[23] The resulting cobaltocenium ion produced in the redox reaction features no appreciable absorption in the visible and near-IR portion (350−1100 nm) of the absorption spectra[39] and thus does not affect our spectra which were obtained in this region.

All of the species in Figure 4 share spectral similarities with those found for the reduced and protonated species of the related dinuclear complex, $[(bpy)_2Ru(tatpp)Ru(bpy)_2]^{4+}$ ($\mathbf{2}^{4+}$),[20,21] (see Chart 1) in which the spectral changes have been attributed to redox and protonation processes localized on the tatpp ligand. Importantly, the visible spectra for $\mathbf{2}^{4+}$ and its protonated and reduced forms are very similar in both acetonitrile and water, providing a simple tool (UV−vis) to follow the speciation in aqueous solution. The same appears to be true for $\mathbf{1}^{2+}$ and its protonated and reduced forms.

For the parent complex $\mathbf{1}^{2+}$, the spectra in MeCN are characterized by an intense band located at 330 nm and a broad but structured band in the region of 435−450 nm. The radical $\mathbf{1}^{\bullet+}$ shows two new absorption bands in the near-IR at 850 nm (weak) and 955 nm (strong), plus a discernible band at 400 nm, as well as a partial bleaching of the absorption at 330 nm. The doubly reduced $\mathbf{1}^{0}$ shows a strong band at 692 nm with a shoulder at 642 nm (see Figure 4a); these two bands are slightly shifted versus those of the doubly reduced dinuclear complex $\mathbf{2}^{2+}$ that appear at 685 and 635 nm.[20] The formation of $\mathbf{1}^{0}$ is also attended by partial bleaching of the 400 nm band.

The absorption spectra for the different species associated with the protonation of $\mathbf{1}^{\bullet+}$ and $\mathbf{1}^{0}$ are shown in Figure 4b. The formation of doubly reduced, single-protonated $\mathbf{H1}^{+}$ is characterized by peaks at 706 and 640 nm plus a faintly discernible shoulder at ca. 605 nm. The doubly reduced, doubly protonated $\mathbf{H_21}^{2+}$ shows a broad band peaking at 565 nm. All of these processes are reversible in the sense that exposure to air reforms the starting complex $\mathbf{1}^{2+}$. For most reduced species, the reoxidation process is fast, taking only seconds. Only $\mathbf{H_21}^{2+}$ is slow, taking several minutes of aerobic exposure to return to the original spectrum.

As seen in Figure 4b, protonation of $\mathbf{1}^{\bullet+}$ gives a spectrum that has features of both $\mathbf{H_21}^{2+}$ and $\mathbf{1}^{2+}$ pointing toward a disproportionation reaction of protonated radical $\mathbf{H1}^{\bullet 2+}$. The spectrum seen in Figure 4b is the same as that

(38) Gubin, S. P.; Smirnova, S. A.; Denisovich, L. I. *J. Organomet. Chem.* **1971**, *30*, 257–265.
(39) Koelle, U.; Infelata, P. P.; Gratzel, M. *Inorg. Chem.* **1988**, *27*, 879–883.

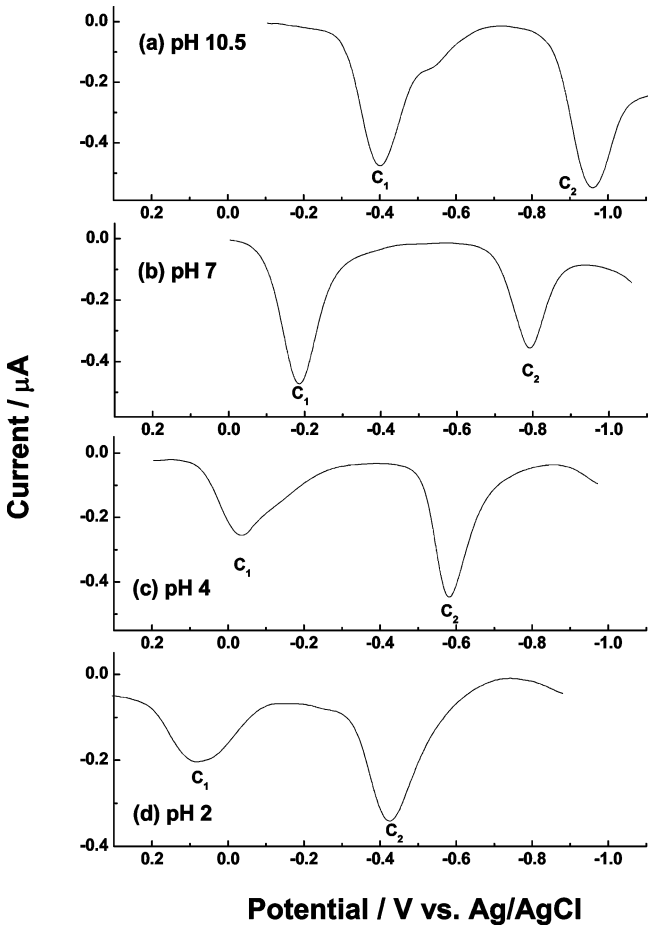

Figure 2. Effect of pH on the differential pulse voltammograms for the electroreduction of $\mathbf{1}^{2+}$ on a glassy carbon electrode (diameter =1.5 mm) in buffered aqueous media. Pulse amplitude = 0.05 V, step size = 0.004 V, pulse duration = 0.05 s, pulse period = 0.2 V. [$\mathbf{1}^{2+}$] = 22 μM (a), 36 μM (b), 36 μM (c), and 28 μM (d).

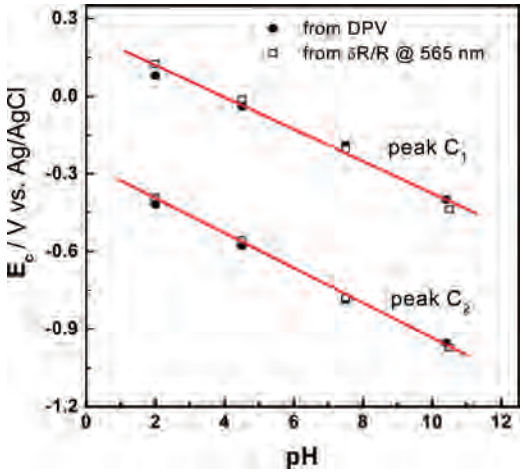

Figure 3. Potential/pH plot for C_1 and C_2 peaks from DPV (Figure 2) and $\delta R/R$ potential plots at 565 nm (data from Figure 7).

seen for a 1:1 mixture of $H_2\mathbf{1}^{2+}$ and $\mathbf{1}^{2+}$, further supporting disproportionation. Furthermore, the closely related dinuclear complex $\mathbf{2}^{4+}$ has been shown to undergo a similar disproportionation after one-electron reduction and protonation, that is, $H\mathbf{2}^{4+}$.[20,21]

C. Spectroelectrochemistry of $\mathbf{1}^{2+}$ in Water. Spectroelectrochemistry provides a method for correlating the

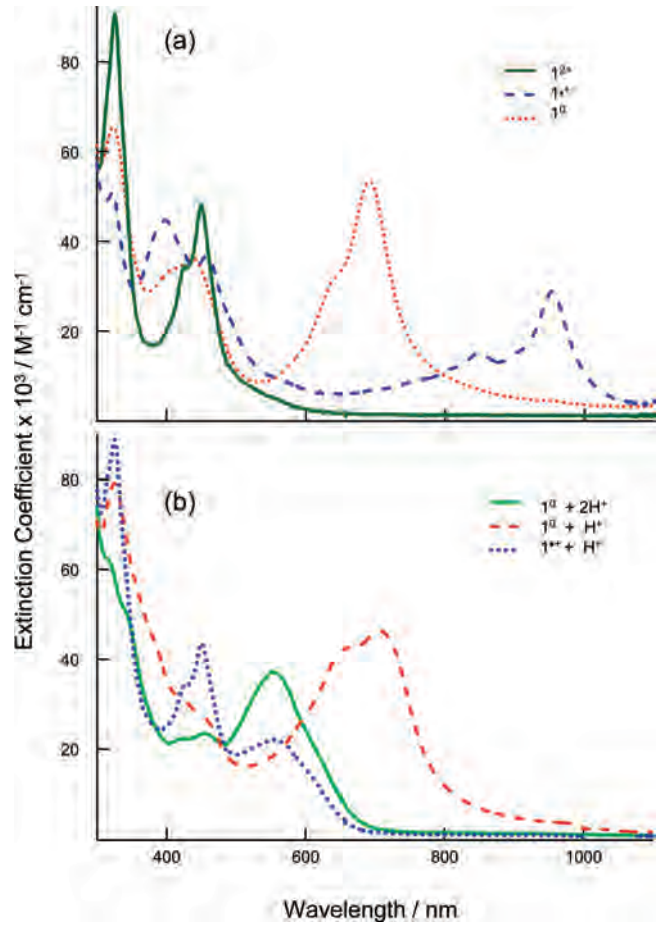

Figure 4. (a) Electronic spectrum (MeCN) of $\mathbf{1}^{2+}$ and the ensuing spectra after the addition of 1 and 2 equiv of cobaltocene, leading to the formation of species $\mathbf{1}^{\bullet+}$ and $\mathbf{1}^{0}$ respectively. (b) Absorption spectra of $\mathbf{1}^{2+}$ after the addition of 2.0 equiv of cobaltocene and 1.0 equiv of TFA (red dash line), 2.0 equiv of cobaltocene and 2 equiv of TFA (green line), and 1.0 equiv of cobaltocene and 1.0 equiv of TFA (blue dot line).

electrochemical processes with the absorption data and thus directly observing the speciation during electroreduction/electro-oxidation processes. Both quasi-steady-state (SS; with a slow potential scan) and DR (with a superimposed potential modulation) spectroelectrochemical measurements were employed because they provide complimentary data. SS data were obtained in the transmittance spectroelectrochemical mode and show all of the species absorbing in the 350−1100 nm range that are generated during a slow potential scan (5 mV/s) in the thin-layer capillary region next to a gold minigrid, whereas DR provides a dynamic, time-dependent picture of the species following the potential modulation in the diffusional layer next to the electrode surface. Figure 5 shows the spectral evolution of $\mathbf{1}^{2+}$ obtained by transmittance during a cyclic potential scan at 5 mV/s in a phosphate buffer solution at pH 10.5 in the −0.1 to −1.2 V potential window. The top two frames (Figure 5a and b) correspond to the negative-going scan (reduction), and the two frames at the bottom (Figure 5c and d) were obtained during the subsequent, positive-going scan (oxidation). Arrows in each frame indicate the evolution of the corresponding spectral peaks with potential. A comparison of the spectra in the negative- and positive-

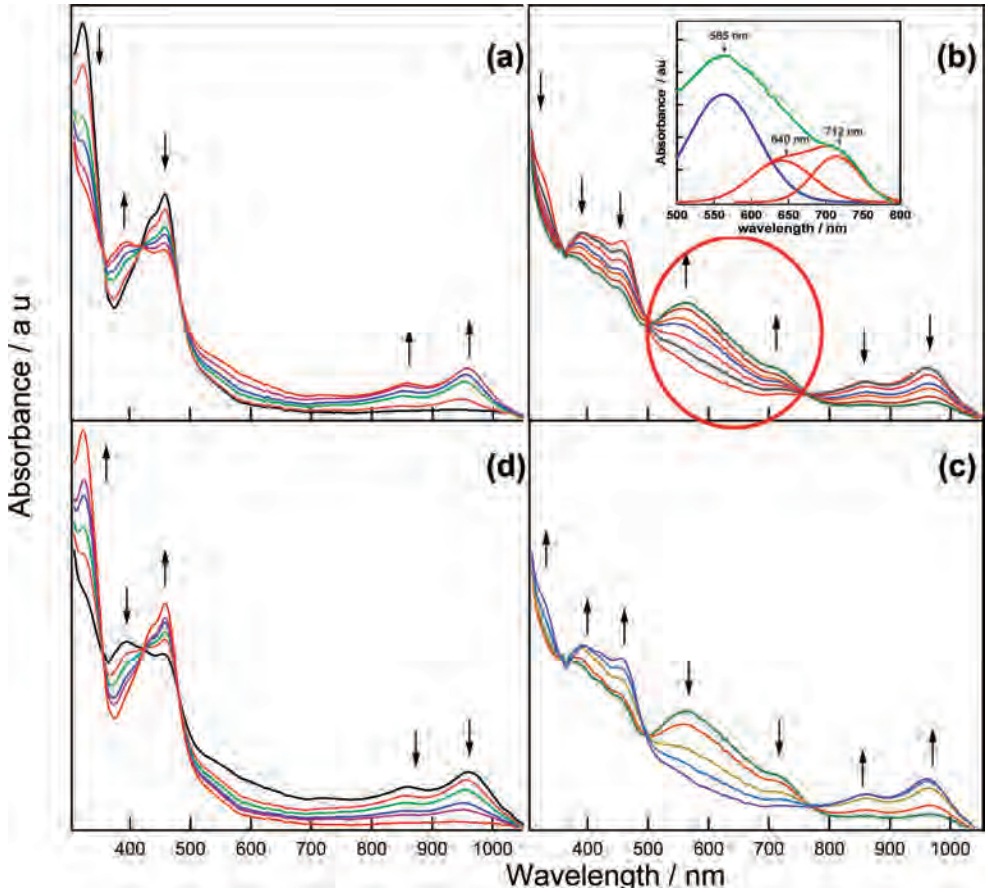

Figure 5. Spectroelectrochemistry of $\mathbf{1}^{2+}$ (150 μM) in a buffered aqueous solution at pH 10.5 using a thin-layer compartment with a gold mesh as the working electrode. Spectra were collected during a cyclic potential scan at 5 mV/s in the −0.1 to −1.0 V potential range. Frames a and b are for reduction and frames c and d for oxidation processes. Insert in b: Peak deconvolution of spectral peaks for $H\mathbf{1}^{+}$ and $H_2\mathbf{1}^{2+}$ species.

going scans shows that the processes are all completely reversible.

Considering each frame in detail, we can see that, in Figure 5a, the first spectrum corresponds to $\mathbf{1}^{2+}$, the starting material, with a sharp band at 330 nm plus another band at 455 nm with a small shoulder at 435 nm. These bands are slightly red-shifted versus the spectrum of $\mathbf{1}^{2+}$ in acetonitrile (Figure 5a), although the spectral profile is quite analogous. During the first electroreduction process, the sharp bands at 330 and 455 nm decrease at the expense of the development of three spectral peaks: a rather broad signature at 400 nm and a pair of sharper bands at 855 and 960 nm. This spectrum is virtually identical although slightly red-shifted (~5 nm) to that obtained by the cobaltocene reduction of $\mathbf{1}^{2+}$ to $\mathbf{1}^{\bullet+}$ (see Figure 4a) and confirms that the two processes (electrochemical and chemical reduction) yield the same product; the slight shift in energy is most likely due to the different solvent.

Figure 5b shows the spectral evolution during the second electroreduction process, where the band pair at 855 and 960 nm is converted into a rather broad band made of contributions from 565, 640, and 712 nm. A comparison with the spectra obtained by cobaltocene reduction and TFA protonation (Figure 4b) reveals that the doubly reduced species are being formed in two different protonation states, $H\mathbf{1}^{+}$ and $H_2\mathbf{1}^{2+}$. In fact, deconvolution of the spectral region between 500 and 800 nm (inserted in Figure 5b for the top curve inside the marked oval) clearly identifies two species, one characterized by two bands at 640 and 712 nm (related to $H\mathbf{1}^{+}$) and the other by a single band at 565 nm (related to $H_2\mathbf{1}^{2+}$). By comparison with the magnitude of the characteristic bands of $H\mathbf{1}^{+}$ and $H_2\mathbf{1}^{2+}$ in Figure 4b, a ratio $H_2\mathbf{1}^{2+}$/$H\mathbf{1}^{+}$ of 7:3 is found. During the potential back scan (Figure 5c and d), the two main reductive processes are seen as completely reversible; that is, the related redox intermediates reappear and disappear in order until $\mathbf{1}^{2+}$ is completely regenerated.

At the other end of the pH range in this study (pH 2), a completely different spectral evolution was found during the slow potential scan from +0.3 to −0.8 V, as seen in Figure 6. Even though this negative-going potential scan encompasses the two voltammetric peaks, C_1 and C_2 (shown in Figure 2d), only a single process is spectroscopically observed and is characterized by the growth of a broad band centered at 568 nm and a shoulder at 640 nm accompanied by a bleaching of the overlapped bands at 455 and 435 nm as well as the peak at 330 nm. The process is clearly not as simple as it first appears given the following observations: (i) the transformation is fastest in the potential range encompassing the C_1 peak and becomes noticeably slower at more negative potentials; (ii) there is a lack of clean isobestic points at ~410 and ~480 nm; and (iii) there is a presence of one neat isobestic point at 347 nm. Importantly, while the baseline rises to a small degree, no bands are seen

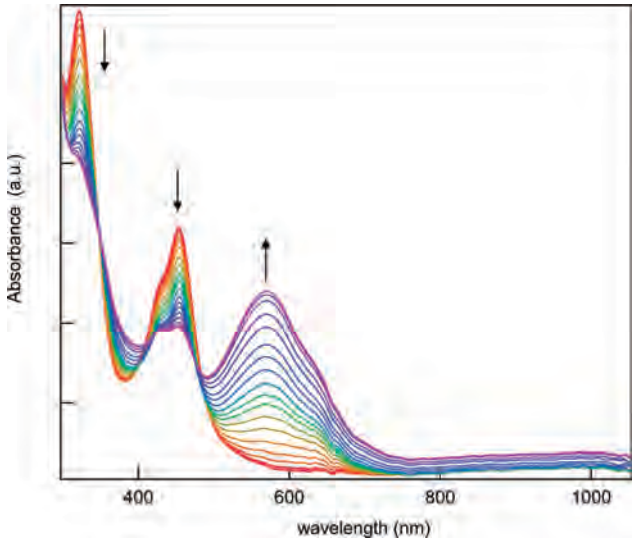

Figure 6. Spectroelectrochemistry of $\mathbf{1}^{2+}$ (120 μM) in a buffered aqueous solution at pH 2 during a negative-going potential scan at 5 mV/s from +0.3 V to −0.80 V. A subsequent positive-going potential scan showed similar spectral profiles occurring in reverse order, and they are not shown for the sake of conciseness. Spectra were obtained in a thin-layer compartment with a gold mesh as the working electrode.

in the near IR region, indicating the absence of the $\mathbf{1}^{\bullet+}$ species. The entire process was reversible with ~90% recovery of the initial spectrum (not shown) during the subsequent positive-going scan.

D. Effect of pH on the DR Profiles of $\mathbf{1}^{2+}$. DR measurements provide a very sensitive detection of reflectance changes (up to 10 ppm) associated with the small amplitude potential modulation of the electrode processes under study.[28,29] The optical signal can be represented by eq 2,[28] in which R is the reflectance, A is the absorbance, and E is the electrode potential.

$$\frac{1}{R}\frac{\delta R}{\delta E} = -\frac{1}{R}\frac{\delta A}{\delta c_{\text{int}}}\frac{\delta c_{\text{int}}}{\delta E} \qquad (2)$$

The magnitude of the $1/R\ \delta R/\delta E$ signal depends on both the kinetic capability of a particular species to follow the potential modulation and its extinction coefficient. The changes of its interfacial concentration (δc_{int}) instigated by the δE potential perturbation are observed through a corresponding change in A. The working electrode provides the potential modulation (source and sink of electrons) and also works as a reflecting mirror for the optical signal. No optical contribution from charge modulation of the electrode was detected, the response being the same when the measurements were conducted on a platinum electrode, which is known to possess an extremely low electroreflectance effect.[40,41] No adsorption reactions or film formation were observed to take place either.

The DR profiles were obtained as a function of the potential at preselected wavelengths chosen from the spectra of the $\mathbf{1}^{2+}$ complex and its redox and protonated congeners (as, for instance, those presented in Figures 5 and 6). With this initial optical data, the DR measurements provide a dynamic optical detection of the various redox and protonation states of the complex in solution as a function of the potential or time. This complements the steady-state spectral information obtained without potential modulation (i.e., that in Figures 5 and 6).

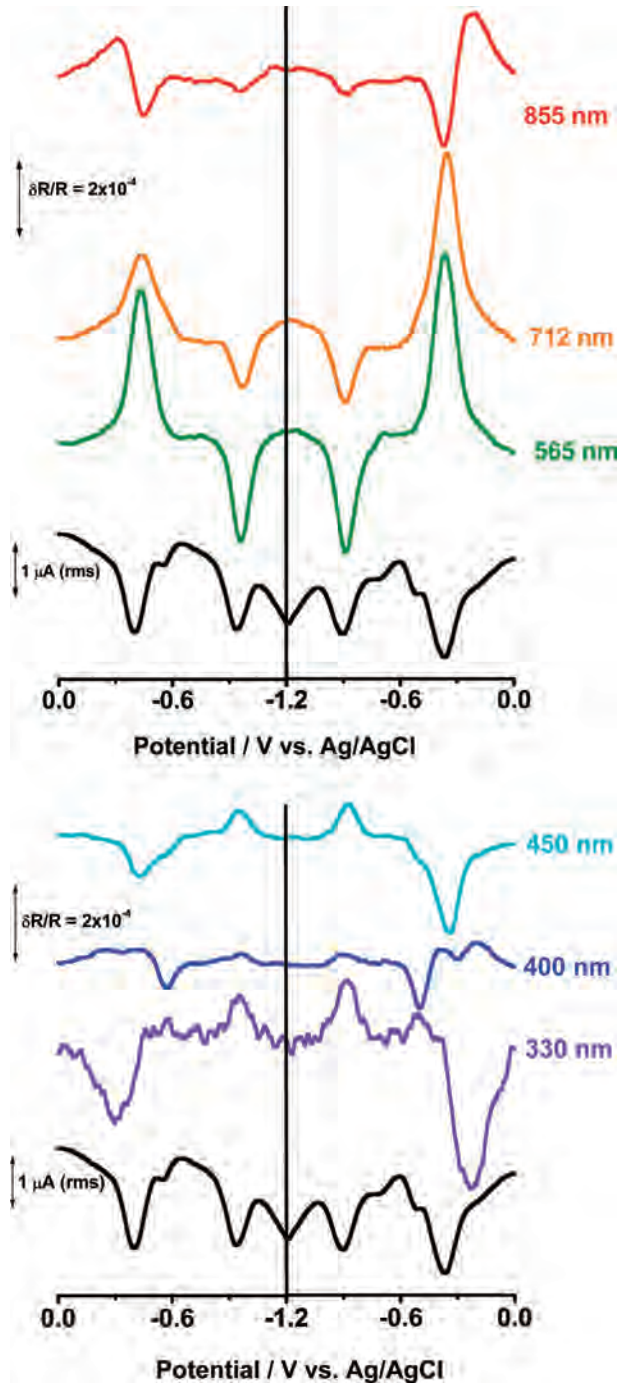

Figure 7. In-phase $\delta R/R$ potential curves for $\mathbf{1}^{2+}$ (20 μM) in a pH 10.5 buffered aqueous solution during a cyclic potential scan on a mirror-polished gold disk electrode. Curves at set wavelengths are shown in cascade to monitor the species involved during the electroreduction processes: 330 and 450 nm for the disappearance of $\mathbf{1}^{2+}$, 855 and 400 nm for the formation of single reduced $\mathbf{1}^{\bullet+}$, and 712 and 565 nm for the double reduced/single protonated $\mathbf{H1}^{+}$ and double reduced/double protonated $\mathbf{H_21}^{2+}$ species. The reversing potential, −1.2 V, vertical dash line, was used to separate the plot into two halves. The corresponding AC voltammograms are at the bottom of the figure for comparison. Both types of measurements (current and $\delta R/R$) were conducted with 50 mV_{p-p} sine waves superimposed on a slow (1 mV s^{-1}) potential scan.

(40) Prostak, A.; Hansen, W. N. *Phys. Rev.* **1967**, *160*, 600–601.
(41) Kolb, D. *J. Phys. Colloq.* **1983**, 137–146.

At pH 10.5, the $\delta R/R$ signals at 855, 712, 565, 450, 400, and 330 nm were recorded during a cyclic potential scan with a superimposed sinusoidal modulation (11 Hz, 50 mV_{p-p}), as shown in Figure 7. For clarity, the potential axis is presented unfolded; in the left frames, the reduction processes (0.0 V → −1.2 V) are plotted, while the right frames contain the oxidation processes observed in the back scan from −1.2 to 0.0 V. The wavelengths were chosen from the data in Figure 5 and are associated with $\mathbf{1}^{2+}$ (450 and 330 nm), $\mathbf{1}^{\bullet+}$ (855 and 400 nm), and $H\mathbf{1}^{+}$ and $H_2\mathbf{1}^{2+}$ (712 and 565 nm, respectively, c.f., Figure 5). Although $H\mathbf{1}^{+}$ has a pair of bands peaking at 640 and 712 nm; the latter wavelength was chosen to monitor $H\mathbf{1}^{+}$ because it has the least overlap with the broad band at 565 nm for $H_2\mathbf{1}^{2+}$. The six $\delta R/R$ plots correspond to the optical response of these four species to the sinusoidal potential wave, while the slow potential scan encompasses the corresponding electroreduction (negative-going scan) and electro-oxidation (positive-going scan) processes. The data are shown in a stacked plot with the AC voltammogram included at the bottom to provide a correlation between optical and electrical signals. In this respect, the AC current can be considered the electrical counterpart to the differential reflectance curves.[28,42] The polarity of the $\delta R/R$ ordinate is such that the appearance and disappearance of the electrochemically generated products are represented by positive and negative components, respectively, for both potential scan directions (positive- or negative-going). In fact, the DR changes do not depend on the direction of the slow potential scan, but only on the δE perturbation.

As can be seen in Figure 7, the first species to appear is $\mathbf{1}^{\bullet+}$ (855 nm), showing a bipolar $\delta R/R$ signal that reaches a maximum at −0.32 V, after which this species is seen disappearing through the negative lobe of the bipolar response. The bipolar signal starts at approximately the same potential as the low preshoulder observed in peak C_1 on the AC voltammogram (see Figure 7, bottom, black trace). The differential reflectance $\delta R/R$ at 712 nm ($H\mathbf{1}^{+}$) is observed to grow slowly even while the 855 nm peak is still increasing, while the 565 signal ($H_2\mathbf{1}^{2+}$) parallels and grows more intense only when the 855 nm absorbance begins to diminish, reaching a maximum at −0.42 V, in agreement with the C_1 current peak. Thus, the DR data are able to decouple the reductive and protonation processes in a more detailed manner than a standard spectroelectrochemical experiment. For example, the peaks corresponding to the appearance of $H_2\mathbf{1}^{2+}$ and $H\mathbf{1}^{+}$ come together as a composite band formed while $\mathbf{1}^{\bullet+}$ disappears in the transmittance spectroelectrochemical experiment (see Figure 5b).

The differential $\delta R/R$ signal at 330 nm (Figure 7) shows a partial bleaching (disappearance) early in the C_1 process and mirrors the 855 nm appearance. However, this peak is not bipolar and is not seen to reappear when the 855 nm peak is bleached. Next, we observe a bleaching of the intensity at 450 nm in the same region where the doubly reduced species $H_2\mathbf{1}^{2+}$ and $H\mathbf{1}^{+}$ are being formed. Finally, the appearance of a small broad peak at 400 nm is observed in the DR data in the negative-going direction, while this change is less unambiguous in the data obtained without potential modulation (compare the data in Figures 5 and 7). However, a bleaching of the absorbance at 400 nm at ∼0.56 V is clear and seems to correlate with the small post-C_1 peak in the AC voltammogram. On the return positive-going scan, the growth and disappearance of the 400 nm peak in the C_1 region is more neatly observed. The discrepancy between the two spectroelectrochemical techniques is due to the sensitivity of DR measurements to transient species, whereas standard spectroelectrochemistry cannot track fast reactions. This suggests that the appearance of the peak at 400 nm in Figure 5 is likely the result of subsequent reactions after initial electroreduction.

In the C_2 region, the DR data show a strong bleaching of the absorbance at 712 and 565 nm, and weaker bleaching at 855 nm. Conversely, the absorbances at 450, 400, and 330 all show small or modest growth during this latter reduction. All of these processes occur at approximately −1.0 V, coinciding exactly with the C_2 peak on the corresponding AC voltammogram. Unlike the processes occurring during the C_1 reduction, all of these changes reflect a simple A → B reaction with just one dominant product in solution. The spectral changes due to the C_2 reductive processes are not seen in the SS spectroelectrochemistry data (Figure 5, frame b). After the C_1 region is passed in the negative-going scan, the peaks at 712 and 565 nm are clearly evident. Upon reaching and passing potentials of the C_2 peak, the 712 and 565 nm peaks are not bleached as seen in the DR data but instead continue to grow in intensity, albeit at a slower rate. The discrepancy in the data between the two techniques is due to their different timescales and is addressed in the Discussion.

Figure 8 shows the DR profiles at three different pHs (10.5, 7.0, and 4.0). Each frame contains three curves related to $\mathbf{1}^{\bullet+}$ (855 nm), $H\mathbf{1}^{+}$ (712 nm), and $H_2\mathbf{1}^{2+}$ (565 nm). For the sake of simplicity, only the negative-going (reducing) potential scans are shown. The reverse scans (not shown) showed reversible behavior at all of the studied pHs. The most telling data here are the observation of a peak at 855 nm for the monoreduced radical $\mathbf{1}^{\bullet+}$ under acidic conditions (pH 4.0). No indication of this peak is seen in the standard spectroelectrochemistry data under acidic conditions, as shown in Figure 6, suggesting no role for the monoreduced species at low pH. The intensity of the $\delta R/R$ signal and the potential window about the bipolar signal (i.e., ∼0.7 V at pH 10 to ∼0.55 V at pH 7 and to ∼0.2 V at pH 4) are clearly pH-dependent, both decreasing with decreasing pH. The dominant species produced during the C_1 process at pH 4 is $H_2\mathbf{1}^{2+}$ as seen by the magnitude of the peak at 565 nm.

At neutral pH (Figure 8b), the DR profiles scanning through the C_1 process show the sequential appearance and disappearance of the radical $\mathbf{1}^{\bullet+}$ accompanied by the appearance of the doubly reduced $H\mathbf{1}^{+}$ and then $H_2\mathbf{1}^{2+}$species. It is interesting to observe that, at this pH, the presence of the monoprotonated $H\mathbf{1}^{+}$ complex is only seen in the potential modulated reflectance measurements, but it is not detected

(42) Brett, C. M. A.; Brett, A. M. O. *Electrochemistry: Principles, Methods, and Applications*; Oxford University Press: Oxford, U.K., 1993.

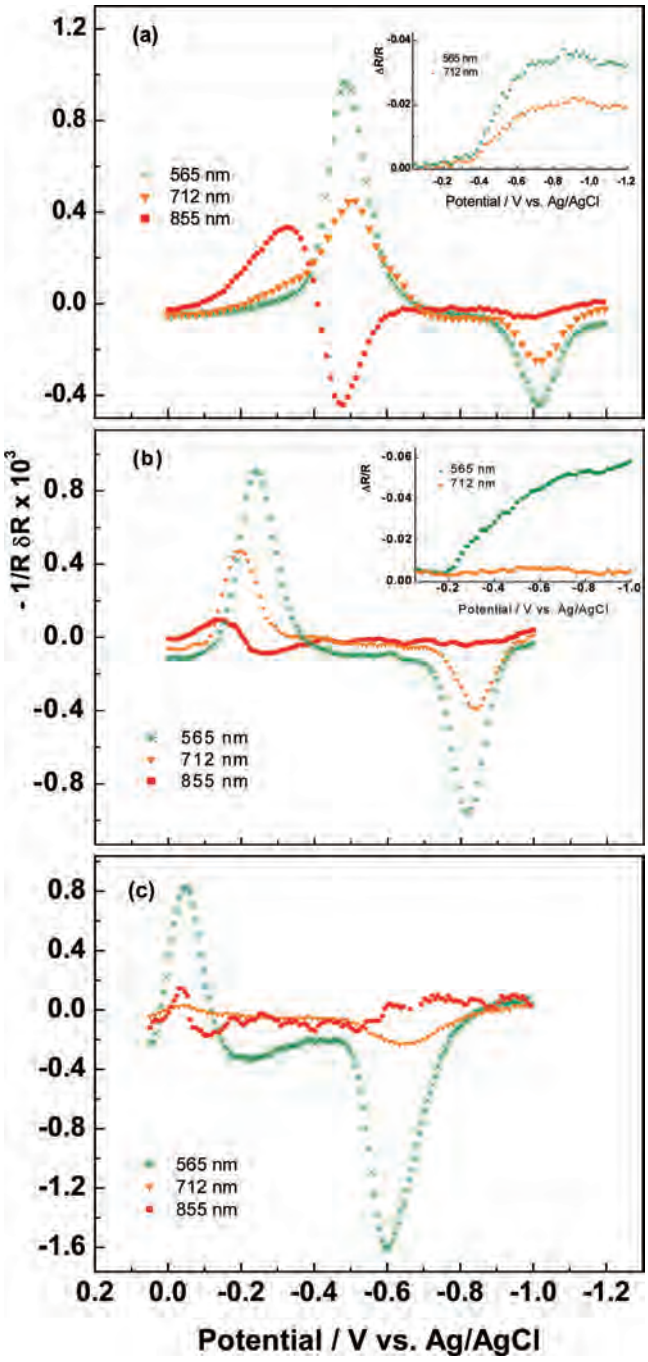

Figure 8. In-phase $\delta R/R$ differential reflectance vs potential curves for $\mathbf{1}^{2+}$ (50 μM) at pH 10.5 (a), 7 (b), and 4 (c), all obtained in the respective buffered aqueous solution. The wavelengths, 855 ($\mathbf{1}^{\bullet+}$), 712 ($\mathrm{H}\mathbf{1}^{+}$), and 565 nm ($\mathrm{H_2}\mathbf{1}^{2+}$), were used at the three pHs. Data acquisition was carried out during a cyclic potential scan, although for simplicity only the negative-going potential scan around processes C_1 and C_2 is presented. Other details are as in Figure 7. Insets: Reflectance measurements at 565 and 712 nm taken without potential modulation at pH 10.5 (a) and pH 7 (b).

in reflectance measurements performed in the same spectroelectrochemical configuration but without superimposed potential modulation (see $\Delta R/R$ profiles in Figure 8b inset). This transitory presence of $\mathrm{H}\mathbf{1}^{+}$ shows the decoupling of electron transfer from proton transfer at faster timescales.

Discussion

The distinct optical spectra of the various redox and protonation states of complex $\mathbf{1}^{2+}$ (see Figure 4) provide a clear tool for following the species involved during its electroreduction in water. The new bands in the absorption spectra have been interpreted in terms of new ligand-centered (LC) transitions on the coordinated tatpp ligand in much the same manner as these transitions were assigned for the dimeric tatpp species $\mathbf{2}^{4+}$.[21] In the parent complex, $\mathbf{1}^{2+}$, two LC bands dominate the visible spectrum, LC_1 at 320 nm and LC_0 which shows a structured band peaking at 450 nm with significant shoulders at 424 and 402 nm. The differences in energy between adjacent peaks are 1363 cm^{-1} and 1290 cm^{-1}, respectively, which, within our ability to accurately determine peaks, are rounded to 1300 cm^{-1} and are typical of the energies associated with aromatic stretching/breathing vibrational modes. The observation of the vibronic fine structure in the electronic spectra is not uncommon in rigid aromatic systems.[43]

These bands are conveniently interpreted in a localized molecular orbital description of the tatpp ligand. LC_0 is assigned as a $\pi-\pi_0^*$ transition (tatpp ligand highest occupied molecular orbital/lowest unoccupied molecular orbital, HOMO−LUMO), whereas LC_1 is a tatpp HOMO to LUMO+1 transition ($\pi-\pi_1^*$). In complex $\mathbf{1}^{2+}$, the LC_0 transition overlaps with the broader Ru(dπ) → ligand (π^*) metal-to-ligand charge-transfer (MLCT) transitions centered at ca. 450 nm, which are typical of Ru(II)-phen and bpy-type complexes. The net result is an intense band peaking at 450 nm with a molar extinction coefficient of 43 300 M^{-1}cm^{-1}.

One- and two-electron reduction to $\mathbf{1}^{\bullet+}$ and $\mathbf{1}^{0}$ strongly perturb the tatpp LC transitions with a partial or full bleaching of the sharp bands at 330 and 450 nm and the appearance of new intense LC bands at longer wavelengths. As the reductions noticeably perturb the tatpp optical transitions (the Ru MLCT transitions are largely unchanged), we can infer that both reductions are localized on the tatpp ligand. Protonation of $\mathbf{1}^{0}$ to $\mathrm{H_2}\mathbf{1}^{2+}$ results in a blue shift of the LC band at 692 to 565 nm, as would be expected from stabilizing some of the tatpp central nitrogen lone pairs.[43]

The radical $\mathbf{1}^{\bullet+}$ is easily identified by the two long wavelength bands at 850 and 955 nm. These peaks are ~1300 cm^{-1} apart in energy and are likely the ν_{0-1} and ν_{0-0} vibronic structures, respectively, of the same electronic transition. Low-energy peaks in the electronic spectra are common for aromatic radical anions,[44] which is how we can view the tatpp portion of the complex in $[(\mathrm{bpy})_2\mathrm{Ru}(\mathrm{tatpp}^{\bullet-})]^{+}$ ($\mathbf{1}^{\bullet+}$). The protonation of $\mathbf{1}^{\bullet+}$ is expected to yield $\mathrm{H}\mathbf{1}^{\bullet 2+}$; however, the spectrum of this species is identical to a 1:1 mixture of $\mathbf{1}^{2+}$ and $\mathrm{H_2}\mathbf{1}^{2+}$, indicative of a disproportonation reaction upon protonation.

Electroreduction Mechanism for Complex $\mathbf{1}^{2+}$ as a Function of pH. From the peak potential versus pH study (Figures 2 and 3), it is possible to assign both of these processes (C_1 and C_2) as being either $1e^-/1H^+$ or $2e^-/2H^+$ processes. The spectroelectrochemical data show the C_1 process to be a $2e^-/2H^+$ process (reaction 3) at all of the pHs examined, as $\mathrm{H_2}\mathbf{1}^{2+}$ is always the dominant product after

(43) Turro, N. J. *Modern Molecular Photochemistry*; University Science Books: Sausalito, CA, 1991.
(44) Fox, M. A. *Chem. Rev.* **1978**, *78*, 253–270.

the C_1 potential region has been scanned. At an inert electrode surface, the only reaction mechanisms possible are ET followed by PT or vice versa (PT−ET). Detailed examination of the differential reflectivity data allows for the determination of some of these mechanistic routes.

The C_1 Process. Reactions 4−10 show a number of elementary steps by which reaction 3 can occur. The terms **E**, **C**, and **DISP**, given in reactions 4−10, are useful ways of describing a sequential mechanism involving both electrochemical and chemical reactions.[45] Reactions involving ET from the electrode surface are indicated with an **E**; first-order or pseudo-first-order (e.g., protonation) chemical reactions are indicated by a **C**; and bimolecular chemical reactions such as disproportionation, dimerization, and comproportionation are indicated by **DISP**, **DIM**, and **COMP**, respectively.

The C_1 overall process (eq 3):

$$\mathbf{1}^{2+} + 2e^- + 2H^+ \rightleftharpoons H_2\mathbf{1}^{2+} \quad (3)$$

$$\mathbf{1}^{2+} + e^- \rightleftharpoons \mathbf{1}^{\bullet+} \quad \mathbf{E} \quad (4)$$

$$\mathbf{1}^{\bullet+} + H^+ \rightleftharpoons H\mathbf{1}^{\bullet 2+} \quad \mathbf{C} \quad (5)$$

$$\mathbf{1}^{\bullet+} + e^- \rightleftharpoons \mathbf{1}^0 \quad \mathbf{E} \quad (6)$$

$$\mathbf{1}^0 + H^+ \rightleftharpoons H\mathbf{1}^+ \quad \mathbf{C} \quad (7)$$

$$H\mathbf{1}^+ + H^+ \rightleftharpoons H_2\mathbf{1}^{2+} \quad \mathbf{C} \quad (8)$$

$$2H\mathbf{1}^{\bullet 2+} \rightarrow \mathbf{1}^{2+} + H_2\mathbf{1}^{2+} \quad \mathbf{DISP} \quad (9)$$

$$H\mathbf{1}^{\bullet 2+} + e^- \rightleftharpoons H\mathbf{1}^+ \quad \mathbf{E} \quad (10)$$

As the mechanism involves a number of PT reactions, the pK_a of these species and pH of the solution will dictate the exact mechanistic pathway. At pH 10.5, the C_1 process is not resolved into separate cathodic peaks; however, it encompasses two reductions that are detected spectroelectrochemically. Both the DR and standard SS spectroelectrochemistry experiments show two stepwise one-electron reductions during the C_1 process producing first $\mathbf{1}^{\bullet+}$ (reaction 4) and then a mixture of $H\mathbf{1}^+$ and $H_2\mathbf{1}^{2+}$. These three species have characteristic and, largely, unique peaks at 855, 712, and 565 nm, respectively. The first reduction is not accompanied by PT (reaction 5) even though the overall C_1 process is a $2e^-/2H^+$ process (see Figure 3).

This monoreduced $\mathbf{1}^{\bullet+}$ product is not appreciably protonated at this basic pH, as evidenced by the DR data, and indicated a pK_a for the corresponding conjugate acid ($H\mathbf{1}^{\bullet 2+}$) of ∼10 or less. The final product distribution shows that the next reduction of $\mathbf{1}^{\bullet+}$ requires first ET followed by PT, as indicated in reactions 6 and 7. $H_2\mathbf{1}^{2+}$ is likely formed predominantly via protonation of $H\mathbf{1}^+$ (reaction 8). Deconvolution of the spectral region between 500 and 800 nm in the standard spectroelectrochemistry data (as shown in Figure 5b, inset) gives the final ratio of $H_2\mathbf{1}^{2+}$ to $H\mathbf{1}^+$ as 7:3 (as measured from the absorbance at 565 for $H_2\mathbf{1}^{2+}$ and at 712 nm for $H\mathbf{1}^+$ after correcting for the differing extinction coefficients). From these data, we determined the pK_{a1} for $H_2\mathbf{1}^{2+}$ to be ∼10.8. These pK_a data are typical for organic radical anions and dianions, with the tatpp radical anion in $\mathbf{1}^{\bullet+}$ being the weaker base compared to the doubly reduced complex $H\mathbf{1}^+$ (e.g., [(bpy)Ru((tatppH$^-$)]$^+$) as the radical has a more extended delocalization of the negative charge over the aromatic framework.[45] With this understanding, we can now describe the overall reaction (reaction 3) for the C_1 process at pH 10.5 as occurring via an **EEC** mechanism for $H\mathbf{1}^+$ and an **EECC** for $H_2\mathbf{1}^{2+}$. As $H_2\mathbf{1}^{2+}$ is the dominant product, this mechanism is largely consistent with an overall $2e^-/2H^+$ process, as shown by the peak shift data for both the DPV data and DR data at 565 nm versus pH (Figure 2).

The post C_1 shoulder at −0.52 V at pH 10.5 (Figure 2) is likely indicative of the dimer formation between the radicals $\mathbf{1}^{\bullet+}$ and $\mathbf{1}^{2+}$ to give $\{\mathbf{1}\}_2^{3+}$ (reaction 11). The radical−substrate dimerization (**RSD**) and radical−radical dimerization (**RRD**) are two subsets of common dimerization (**DIM**) mechanisms. Reaction 11 corresponds to a **RSD** mechanism, and the resulting species then undergoes further reduction at the later potential, as seen in reaction 12. Dimer formation was observed to be the dominant process in an aprotic solvent (MeCN) and caused a splitting of the C_1 peak into two peaks, the latter of which is coincident with the post-C_1 shoulder seen here. This dimer $\{\mathbf{1}\}_2^{3+}$ reduction (reaction 12) is not accompanied by protonation and therefore is observed at a more negative potential. Furthermore, the product $\{\mathbf{1}\}_2^{2+}$ only achieves a net two-electron reduction (one electron per $\mathbf{1}^{2+}$ unit) as the electronic structure is significantly modified by dimerization. The summation of reactions 4, 11, and 12 gives an **E**−**RSD**−**E** mechanism. An alternative explanation would be the formation of $\mathbf{1}^0$ in two one-electron steps, with the C_1 postshoulder as one of the steps. This can be ruled out, as the dominant products shown by spectroelectrochemistry are $H_2\mathbf{1}^{2+}$ (70%) and $H\mathbf{1}^+$ (30%). Given this product distribution, the pK_a for $H\mathbf{1}^+$ must be significantly higher than 10.5.

$$\mathbf{1}^{\bullet+} + \mathbf{1}^{2+} \rightarrow \{\mathbf{1}\}_2^{3+} \quad \mathbf{RSD} \quad (11)$$

$$\{\mathbf{1}\}_2^{3+} + e^- \rightleftharpoons \{\mathbf{1}\}_2^{2+} \quad \mathbf{E} \quad (12)$$

At the same pH, the dominant product for electroreduction of the dinuclear complex $\mathbf{2}^{4+}$ is the doubly reduced, singly protonated complex [(bpy)$_2$Ru^{2+}(tatppH$^-$)Ru^{2+}(bpy)$_2$]$^{3+}$ ($H\mathbf{2}^{3+}$) obtained via an **EEC** mechanism.[21] The presence of the second Ru^{2+} ion in $\mathbf{2}^{4+}$ lowers the pK_a of the corresponding species [(bpy)$_2$Ru^{2+}(tatppH$^-$)Ru^{2+}(bpy)$_2$]$^{3+}$ ($H\mathbf{2}^{3+}$) and [(bpy)$_2$Ru^{2+}(tatppH$_2$)Ru^{2+}(bpy)$_2$]$^{4+}$ ($H_2\mathbf{2}^{4+}$) to ∼10 and 9.0, respectively (for deprotonation of the tatpp unit). In contrast, the pK_a for the related mononuclear species [(bpy)$_2$Ru^{2+}(tatppH$_2$)]$^{2+}$($H_2\mathbf{1}^{2+}$) is 10.8 (vide supra). The increase in acidity in $H_2\mathbf{2}^{4+}$ over $H_2\mathbf{1}^{2+}$ is due, in part, to the higher overall positive charge of the former species. Furthermore, coordination to the second Ru(II) center in $H_2\mathbf{2}^{4+}$ can result in greater overall electron delocalization for the tatppH$_2$ unit, further lowering the pK_a. This second ion effect is also seen in the electrochemical data, as the first reduction $\mathbf{2}^{4+/3+}$ is positive compared to that of the $\mathbf{1}^{2+/+}$

(45) Savéant, J.-M. *Elements of Molecular and Biomolecular Electrochemistry -An Electrochemical Approach to Electron Transfer Chemistry*; Wiley-Interscience: Hoboken, NJ, 2006.

couple by 150 mV. A drop of ~1.8 pH units is observed on going from one Ru center in $H_2\mathbf{1}^{2+}$ to two Ru centers in $H_2\mathbf{2}^{4+}$ for the same acid dissociation reaction (i.e., tatppH$_2$ → tatppH$^-$ + H$^+$). Assuming that this pH difference is relatively constant for all three pK_a's involved, we can further narrow the approximate pK_a's for $H\mathbf{1}^{\bullet 2+}$ and $H\mathbf{1}^{+}$ to ~9.8 and 11.8, respectively.

At pH 2, the SS spectroelectrochemical data in the C_1 potential region show a smooth transition from $\mathbf{1}^{2+}$ to $H_2\mathbf{1}^{2+}$ without any observable intermediates, as seen in representative spectra shown in Figure 6 at pH 2. However, the putative isobestic points at ~410 and ~480 nm are not stationary, and the DPV becomes significantly broadened (Figure 2), indicating a more complex reaction. Under acidic conditions, the predominant pathway to formation of $H_2\mathbf{1}^{2+}$ appears to involve an **EC−DISP** mechanism consisting of reactions 4, 5, and 9. As seen in Figure 8c for pH 4, the DR peak indicative of $H_2\mathbf{1}^{2+}$ formation (at 565 nm) is observed first, with a small DR signal for the monoreduced product at 855 nm only observed when the rate of $H_2\mathbf{1}^{2+}$ formation is reaching its apex. Reaction 9 generates both $H_2\mathbf{1}^{2+}$ and $\mathbf{1}^{2+}$ at the electrode interface but the $\mathbf{1}^{2+}$ is rapidly "rereduced" (reaction 4) at these negative potentials. Protonation regenerates more $H\mathbf{1}^{\bullet 2+}$ species, which can then undergo disproportionation (reaction 9). The largest buildup of $\mathbf{1}^{\bullet +}$ in such a sequence would coincide with the maximal rate of $H_2\mathbf{1}^{2+}$ formation, as seen in Figure 8c for the 565 and 855 nm traces. Disproportionation reactions are extremely common when electrochemically generated species are chemically converted to unstable species.[45]

At an intermediate pH, i.e. pH 7, two mechanisms seem likely. First, as we are well below the approximate pK_a of 9.8 for $H\mathbf{1}^{\bullet 2+}$, reactions 4 and 5 occur to generate $H\mathbf{1}^{\bullet 2+}$. This is seen in the positive potential shift of the bipolar signal for the 855 nm absorbance as the pH is lowered. This species, $H\mathbf{1}^{\bullet 2+}$, can then either disproportionate (reaction 9) or be further reduced by the electrode (reaction 10) and then protonated (reaction 8). The overall reaction mechanism for both paths is thus either **EC−DISP** or **ECEC**. The appearance of the transient species in the order $\mathbf{1}^{\bullet +}$ (855 nm) first, then $H\mathbf{1}^{+}$ (712 nm), and finally $H_2\mathbf{1}^{2+}$ (565 nm), as seen in Figure 8b, suggests that the latter is at work at pH 7. In comparison with the broadened asymmetric DPV profile for the C_1 process at pH's 4 and 2, the DPV data at pH 7 appear as a narrow single peak. These differences may be indicative of a switch from the **ECEC** mechanism at pH 7 to the **EC−DISP** at pH's 4 and 2. It is important to note that we never observe $H\mathbf{1}^{+}$ in any appreciable amount at pH 4 (Figure 8c), which would lend support to the **EC−DISP** mechanism at these lower pHs. The disproportionation reaction (reaction 9) has been demonstrated chemically by protonation of $\mathbf{1}^{\bullet +}$ in MeCN, as shown in Figure 4b.

The C_2 Process. At every pH investigated, the spectroelectrochemical data for the C_2 process obtained without potential modulation do not show significant changes in the absorption spectrum of the species generated in the C_1 process. The only observation is a continual buildup of the doubly reduced products (see Figures 5 and 6 and inserts in Figure 8a and b). However, bleaching of the optical bands for $H\mathbf{1}^{+}$ and $H_2\mathbf{1}^{2+}$ is clearly seen in potential modulated data (Figures 7 and 8). The discrepancy in the data between the two techniques shows the difficulty in interpreting data from the SS spectroelectrochemical experiment. If the rate of diffusion of $\mathbf{1}^{2+}$ from the bulk solution into the capillary region is faster than the spectral time frame (seconds for SS techniques), then the electroreduced product is free to react with the bulk species, leading to other products resulting from comporportionation reactions (**E−COMP** mechanism), as shown in Figure 1. The faster DR technique (time scale < 0.1 s) is therefore able to decouple the aforementioned **E−COMP** process.

As the E_c versus pH plot (Figure 3) indicates that the C_2 peak encompasses a two-electron/two-proton process (e.g., reaction 13), the DR data only reveal that both $H\mathbf{1}^{+}$ and $H_2\mathbf{1}^{2+}$ are consumed in this C_2 process. The mechanistic details of reaction 13 are not revealed in any of the data, indicating that these reactions are faster than the time scale of the DR measurement. The product or reaction 13, $H_4\mathbf{1}^{2+}$, would not be expected to show any visible absorption bands due to the high degree of saturation of the tatpp ligand, and thus no new bands are correlated with its appearance. This was seen in the related dinuclear complex $H_4\mathbf{2}^{4+}$, which, when generated electrochemically, shows a bleaching of all of the visible LC bands.[21] The observation of a continual buildup of $H_2\mathbf{1}^{2+}$ in the SS spectroelectrochemical experiment supports the formation of $H_4\mathbf{1}^{2+}$, assuming that this species is rapidly consumed in a comproportionation reaction (shown in reaction 14 and in Figure 1) with $\mathbf{1}^{2+}$ in the bulk.

$$H_2\mathbf{1}^{2+} + 2e^- + 2H^+ \rightleftharpoons H_4\mathbf{1}^{2+} \tag{13}$$

$$H_4\mathbf{1}^{2+} + \mathbf{1}^{2+} \rightarrow 2H_2\mathbf{1}^{2+} \quad \textbf{COMP} \tag{14}$$

Conclusions

The mononuclear complex $\mathbf{1}^{2+}$ shows a rich redox chemistry with up to four reversible tatpp-based reductions. In aqueous media, these four redox processes occur predominantly as two two-electron/two-proton processes, C_1 and C_2, in the pH range 10.5−2. The mechanism of the C_1 process was shown to change dramatically as a function of the pH. Under basic conditions, the complex undergoes two sequential one-electron reductions followed by one (**EEC**) or two protonations (**EECC**), depending on the exact pH. Acidic conditions favor an **EC−DISP** mechanism in which initial electrochemical reduction is followed by protonation and then disproportionation of the protonated radical, $H\mathbf{1}^{\bullet 2+}$. At neutral pH, a third mechanism seems to be involved in which the formation of $H\mathbf{1}^{\bullet 2+}$ is followed by electrochemical reduction and then protonation—an overall **ECEC** mechanism. At all of the pH's examined, the C_2 process reflects a double reduction and double protonation occurring at timescales faster than our ability to detect the individual ET and PT steps, leaving the mechanistic details unknown. The product, $H_4\mathbf{1}^{2+}$, is not observed because of a rapid comproportionation reaction with $\mathbf{1}^{2+}$ (present in the bulk) but is

inferred by a bleaching of the DR signals for $H_2\mathbf{1}^{2+}$. This is consistent with the SS data, which show a continual buildup of $H_2\mathbf{1}^{2+}$ as predicted by reaction 14.

This paper shows the advantages and insights that can be gained using a combination of standard and potential modulated spectroelectrochemistry to follow stable "equilibrium" species as well as transient species. Without the latter technique, the detailed mechanism of these overall two-electron/two-proton processes would not be easily determined. An understanding of these mechanistic details provides a framework by which to describe and potentially modify the unusual multielectron-accepting capabilities of tatpp and related ligands. Further work is in progress to explore homogeneous electron transfer steps such as comproportionation and disproportionation reactions, occurring during the reduction of complex $\mathbf{1}^{2+}$.

Acknowledgment. We thank the National Science Foundation CHE-0518649 (FMM, NRT), the Robert A. Welch Foundation Y-1301(FMM), and BID 1728/OC-RA, PICT #26195/04 (ROL) for support of this research. We thank the reviewers for their helpful comments on clarifying the discussion section of this manuscript.

IC8009157